Journal of Alloys and Metallurgical Systems 9 (2025) 100155

Contents lists available at ScienceDirect

Journal of Alloys and Metallurgical Systems

journal homepage: www.journals.elsevier.com/journal-of-alloys-and-metallurgical-systems

Corrosion evaluation and microstructural characteristics of 70/30 copper-nickel alloy fabricated by laser powder bed fusion

Mahdi Nadimi [a], Jie Song [b,*], Lin Cheng [c], Yao Fu [a,d,*]

[a] Department of Aerospace and Ocean Engineering, Virginia Polytechnic Institute and State University, USA
[b] College of Engineering, SUNY Polytechnic Institute, USA
[c] Department of Mechanical Engineering, University of Maryland, USA
[d] Department of Materials Science and Engineering, Virginia Polytechnic Institute and State University, USA

ARTICLE INFO

Keywords:
Corrosion properties
Laser powder bed fusion
Cu-Ni alloy
Microstructure
3.5 wt% NaCl

ABSTRACT

This study explored the fabrication of 70/30 Cu-Ni via LPBF technique and investigated its corrosion and microstructure properties. Samples were fabricated with varied parameters, including power, scan rate, and hatch spacing, and compared with wrought Cu-Ni alloy. Corrosion behaviour was conducted using cyclic polarization and EIS in 3.5 wt% NaCl. Optical microscopy and EBSD techniques were employed for microstructure evaluation. The results revealed that the examined LPBF samples had surface porosities below 1 %, indicating superior density and minimal voids, with larger grain sizes displaying elongated grain. Additionally, LPBF samples exhibited delayed breakdown passive layer potential, superior repassivation abilities compared to the wrought specimen. EIS analysis revealed corrosion resistance of as-fabricated samples was slightly higher than conventional ones, peaking at 58–73 kΩ.cm^2 with hatch spacing between 125 and 200 μm and P/V ratio between 1.7 and 2 J/mm. However, deviation in parameters led to a decrease in corrosion resistance.

1. Introduction

Copper is a versatile metal that has been utilized for ages. It is a popular industrial metal because of its excellent ductility, malleability, thermal and electrical conductivity [1]. Although its outstanding characteristics are undeniable, when it comes to corrosion performance in seawater, it is considered one of the least resistant metals. Adding nickel to copper as an alloying element solves that problem and even increases the strength resistance. Cupronickel or Cu-Ni alloys are widely utilized in maritime environments for pipelines, structural materials, and ship hulls due to their corrosion resistance, mechanical ductility, outstanding electrical and thermal conductivity, and excellent anti-fouling qualities [2,3]. When Cu-Ni alloys are exposed to corrosive solution, each nickel ion (Ni^{2+}) replaces two copper ions (Cu^{+}) resulting in the making of a strong protective film on the surface. Aside from that, duplex oxides such as Cu-hydroxide layer can also protect the alloy from corrosion [4]. That is why this alloy is well known for its corrosion resistance.

Among Cu-Ni alloys, 70/30 Cu-Ni alloy stands out as the most extensively used in critical components subjected to harsh environments. The remarkable corrosion resistance of Cu-Ni alloys primarily arises from the development of a protective corrosion product layer on the surface, which effectively impedes ion diffusion [5,6]. According to North et al. [7], investigation into the corrosion characteristics of pure copper and Cu-Ni alloys in terms of the defective semiconductor properties of the Cu_2O film formed on the samples, the concentration of cation vacancies in the copper oxide layer was reduced when nickel ions occupied the vacancies, increasing the corrosion resistance. Due to the many applications and the production need, its production with conventional methods is less economical, especially when the shape of the piece is twisted [8].

Additive manufacturing process has transformed industries by reducing waste and expanding design possibilities. It was initially used for prototyping but has now expanded to include a wide range of applications, particularly commercial product manufacturing [9]. Challenges such as poor mechanical qualities are being solved through continual research and material improvements, showing the technology's dynamic nature [10–12]. Another advantage of this technology is that it produces higher-performing part while reducing the weight of complex components that are difficult to fabricate with conventional machining [10].

* Corresponding author.
* Corresponding author at: Department of Aerospace and Ocean Engineering, Virginia Polytechnic Institute and State University, USA.
E-mail addresses: jie.song@sunypoly.edu (J. Song), yaof@vt.edu (Y. Fu).

https://doi.org/10.1016/j.jalmes.2025.100155
Received 21 November 2024; Accepted 13 January 2025
Available online 14 January 2025

Nowadays many different parts can be fabricated using advanced manufacturing (AM) techniques. Each AM technique is used for different purposes, but the most popular ones are laser powder bed fusion (LPBF) [13], electron beam powder bed fusion (EBPF) [14] and direct energy dispersion (DED) [15]. Among all of them, LPBF can produce objects with excellent resolution and a superior surface polish [16,17]. Shortly, this process starts with spreading a thin layer of metal powders over a desired area and a laser accurately scans the area and then begins to melt the powders. After solidification of the first layer, a new powder layer is spread and the procedure repeats [13,18].

Numerous studies have been conducted on Cu-Ni. Badawy et al. [19] found that increasing Ni content in Cu–Ni alloys reduces the corrosion rate in neutral chloride solutions, while higher chloride concentration initially raises the corrosion rate but decreases above 0.3 mol/dm^{-3} due to passive film formation. Electrochemical techniques and impedance spectroscopy indicated improved corrosion resistance with higher Ni content and longer immersion times. Ekerenam et al. [20] investigated the surface of 90/10 Cu-Ni alloy after six months of seawater immersion and found that a multilayer structure of corrosion products significantly contributed to erosion corrosion resistance. They also observed that with increasing flow velocity, the surface film, consisting of an inner layer of Cu_2O doped with Ni^{3+} and Ni^{2+}, formed a strong bond with the substrate and was capable of self-repair. Although quite a few studies have been conducted on this alloy, there remains a significant gap in research concerning its manufacturability by AM techniques and resultant corrosion properties. Most existing literature focuses on the basic characteristics and traditional applications of the alloy, leaving a need for more in-depth investigation into how modern manufacturing processes affect its performance. Understanding these aspects is crucial for optimizing the alloy's usage in contemporary engineering and industrial applications, particularly in environments where corrosion resistance is a key factor. Yugang et al. [21] employed wire arc additive manufacturing (WAAM) to create a gradient Cu-Ni alloy and investigated its material properties. Their findings revealed that incorporating nickel into the gradient layers reduced the average grain size but resulted in the emergence of unusually large secondary grains. This alteration influenced grain orientation, texture composition, microhardness, and tensile strength, which initially increased with the nickel content, peaked, and then declined.

In earlier research, our group explored the microstructural characteristics and corrosion performance of 70/30 Cu-Ni alloy produced using wire arc [22] and in this study, we aim to use LPBF as another AM process to fabricate 70/30 Cu-Ni alloy, examining the effects of parameters such as hatch spacing, laser power, and scan rate on microstructure and electrochemical behavior. The results will be compared to those of a conventional 70/30 Cu-Ni wrought sample to elucidate the unique characteristics and potential advantages of LPBF-produced alloys.

2. Experimental

2.1. Material preparation and LPBF process

In this investigation, a SLM 280 machine equipped with a single laser 400 W Tank Feed was used to fabricate LPBF samples. The powder utilized was 70/30 Cu-Ni (C96400) from Sandvik Osprey LTD, with particle diameters ranging between 15 and 45 μm.

As previously described, the LPBF method fabricates samples layer by layer. Initially, a powder layer with a thickness of 30 μm (t) is applied to a pre-heated substrate. Then, a high-powered laser scans the cross-section of the part design, melting and fusing the powder particles to form a solid layer. Subsequently, a new layer of powder is spread over the previous layer, and the procedure repeats until the entire part is completed. A scanning strategy was employed following a rotation of 67° after every layer and the build direction was designated as the Z direction, making the XY plane the horizontal plane, as illustrated in Fig. 1.

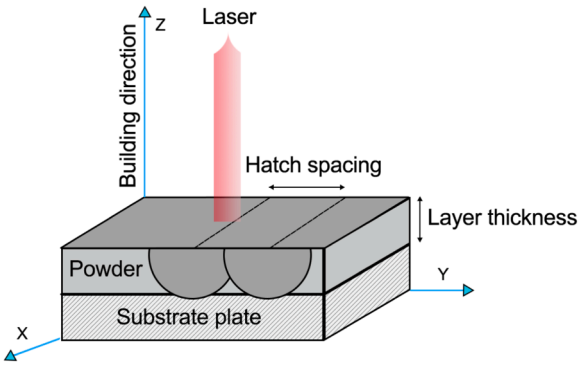

Fig. 1. LPBF process and orientation of Cu-Ni samples.

To evaluate the effects of printing parameters, over a hundred samples were fabricated with power settings ranging from 300 to 400 W, scan rates from 200 to 600 mm/s, and hatch spacings from 50 to 400 μm and only those that exhibits minimal lack-of-fusion defects were further analyzed. The laser power (P), scanning speed (V), and hatch spacing (H) along with volume energy density (VED $= \frac{P}{V.H.t}$) of defect-minimized samples are presented in Table 1.

2.2. Microstructural analysis

To gain a comprehensive understanding of how printing conditions affect microstructural variations, both optical microscopy (OM) and electron backscatter diffraction (EBSD) techniques were utilized. The first technique provides a broad overview of the microstructural features like porosity and overall sample integrity [23]. Micrographs were taken from four separate areas on each sample to evaluate porosity for increased accuracy, and all images were analyzed using ImageJ software. Meanwhile, EBSD offers detailed insights into the crystallographic orientation and phase distribution within the samples [24]. By combining these two methods, a thorough analysis of the microstructural changes induced by different printing parameters was achieved. For this analysis, both the as-fabricated and conventional samples were cut into square prism shapes with 10 × 10 × 5 mm dimensions using electrical discharge machining (EDM) machine and then sectioned in a direction perpendicular (XY plane) and parallel (YZ plane) to the fabrication axis. After cutting, the samples were mounted in epoxy molds to stabilize and protect them during subsequent preparation steps. The mounted samples were then subjected to a series of grinding stages using silicon carbide (SiC) papers followed by polishing with 3 μm colloidal silica suspension as the final stage for OM analysis. For EBSD analysis, electropolishing was conducted in 15 % sulfuric acid and 85 % methanol at room temperature, further refining the surface by removing a thin material layer and enhancing microstructural visibility.

2.3. Electrochemical test

All electrochemical tests were performed using a three-electrode setup. In this setup, the test samples served as the working electrode, the Ag/AgCl electrode as the reference, and a graphite plate acted as the counter electrode. Prior to testing, all XY-plane specimens were mounted with an exposure area of 0.3 cm^2 and ground with silicon carbide (SiC) papers up to 2500 grit to ensure a smooth surface. Initially, the samples were immersed in 3.5 wt% NaCl for up to 3 h for open circuit potential (OCP) stabilization. Following this, cyclic potentiodynamic polarization (CPP) tests were carried out with a scan rate of 0.166 mV/s, starting from −250 mV below OCP. The reverse scan began when the current density reached 1 mA/cm^2 during forward scan. This process helped in evaluating the corrosion resistance and passivation behaviour of all samples.

Table 1
The LPBF parameters for different samples.

Sample	Power (W)	Scan rate (mm/s)	Hatch spacing (μm)	VED (J/mm^3)
1	400	200	175	381.0
2			200	333.3
3			225	296.3
4			250	266.7
5			275	242.4
6			300	222.2
7			325	205.1
8			350	190.5
9			375	177.8
10			400	166.7
11	400	300	50	888.9
12			75	592.6
13			100	444.4
14	400	400	100	333.3
15			200	166.7
16	400	600	100	222.2
17	375	200	100	625.0
18			125	500.0
19			150	416.7
20			175	357.1
21			200	312.5
22			225	277.8
23			250	250.0
24			275	227.3
25			300	208.3
26			350	178.6
27			400	156.3
28	375	300	50	833.3
29	350	200	125	466.7
30			150	388.9
31			175	333.3
32			200	291.7
33			225	259.3
34			250	233.3
35			275	212.1
36			300	194.4
37			325	179.5
38			350	166.7
39	350	300	50	777.8
40		400	100	291.7
41			150	194.4
42	325	200	75	722.2
43			100	541.7
44			125	433.3
45			150	361.1
46	300	200	125	400.0
47			150	333.3
48			175	285.7

Electrochemical impedance spectroscopy (EIS) was conducted to further characterize the electrochemical properties of the system. This test was performed with AC amplitude of 10 mV/s over a frequency range from 10^{-2} to 10^{5} Hz. The EIS technique provided insights into the resistive and capacitive behavior of the protective films formed on the sample surfaces.

The electronic properties of the films on Cu-Ni alloys were investigated using the Mott-Schottky (MS) technique. This method involved measuring the capacitance of the oxide films at a fixed frequency of 1 kHz while incrementally varying the applied potential from 0 to −0.3 V vs. OCP in steps of 10 mV. The MS technique helped determine the donor density of the semiconductor oxides, which is a critical parameter for understanding the corrosion behavior.

To ensure the reliability and accuracy of the results, all electrochemical tests were repeated three times. Notably, the EIS and MS measurements were carried out after OCP stabilization and separately from the CPP.

3. Results

3.1. Optical microscopy analysis

OM images of the samples with laser power of 375 W, scan rate of 200 mm/s, and different hatch spacing values are shown in Fig. 2. The black areas represent the gas pores and/or unfused pores. As is seen in Fig. 2a-g, there is no direct relationship between hatch spacing and the presence of pore defects. The sample created with a hatch spacing of 150 μm had the fewest number of defects indicating a denser and high-quality structure. As the hatch spacing increased to 250 μm, the pore size within the material also increased, with some pores reaching nearly 100 μm (Fig. 2d). Interestingly, when the hatch spacing was increased beyond 250 μm, there was a noticeable reduction in defect formation. Thus, departing from a threshold hatch spacing likely alters the way melting and cooling processes in such a way that it limits pore generation, although this may come at the expense of other aspects of material quality.

The defects on the surfaces are formed as a result of inadequate or excessive input energy. The lack of sufficient energy prevents proper fusion between scan paths, leading to incomplete bonding and the formation of unfused pores that are irregular in shape. In contrast, when the energy input is excessively high, metal vapor becomes trapped within the molten pool, resulting in the formation of small, spherical cavities known as gas pores [25,26].

As demonstrated in Fig. 2a'-g', on the YZ plane, due to overlapping melt pools created by the sequential usage of laser energy along with layer wise scanning, a stepped molten path is formed at a particular angle perpendicular to the building direction. A good example of unfused pores can be seen in some areas of sample H200. The presence of these pores indicates that there may have been insufficient overlap between the laser passes, inadequate energy input, or other factors affecting the consistency of the melt pool, ultimately compromising the sample's overall structural integrity.

The porosity percentage of all LPBF samples measured by using a black-and-white contrast of the optical micrographs in ImageJ software is presented in Fig. 3. In this figure, the vertical axis represents the linear energy density, which is the ratio of laser power (P) to scan speed (V) and the horizontal axis shows the hatch spacing (H). This illustrates how changes in energy density and hatch spacing influence the degree of porosity in the material. The key findings of this graph are that the porosity percentage for all samples was below 1 % spanning from 0.45 % to 0.95 %, which means all of them had a relatively high density and minimal voids. Although there were slight differences in porosity, the samples with linear energy densities (P/V) between 1.1 and 1.75 J/mm, combined with hatch spacings between 50 and 325 μm, achieved the lowest void fraction, with porosity levels below 0.6 %. This trend is highlighted in three different areas circled in Fig. 3.

In contrast, when the hatch spacing is increased beyond this range, the porosity percentage increased ($P > 0.6$ %). This is due to insufficient energy input and poor overlap between the scan paths, leading to incomplete melting and higher occurrences of voids and defects. These conditions result in a less dense and structurally weaker material, highlighting the importance of carefully optimizing the process parameters to achieve the desired material properties.

3.2. EBSD analysis

The EBSD grain structure and inverse pole figures (IPF) of both conventional and as-fabricated samples are shown in Fig. 4. It is evident that the grain size of the conventional sample (Fig. 4a) is considerably smaller than that of the as-fabricated samples (Fig. 4b-h). Additionally, the grains in the conventional sample exhibit an equiaxed grain texture, indicating uniformity in their dimensions. In contrast, the as-fabricated samples predominantly exhibit elongated and irregular grain morphologies, primarily oriented towards the $< 101 >$ crystallographic

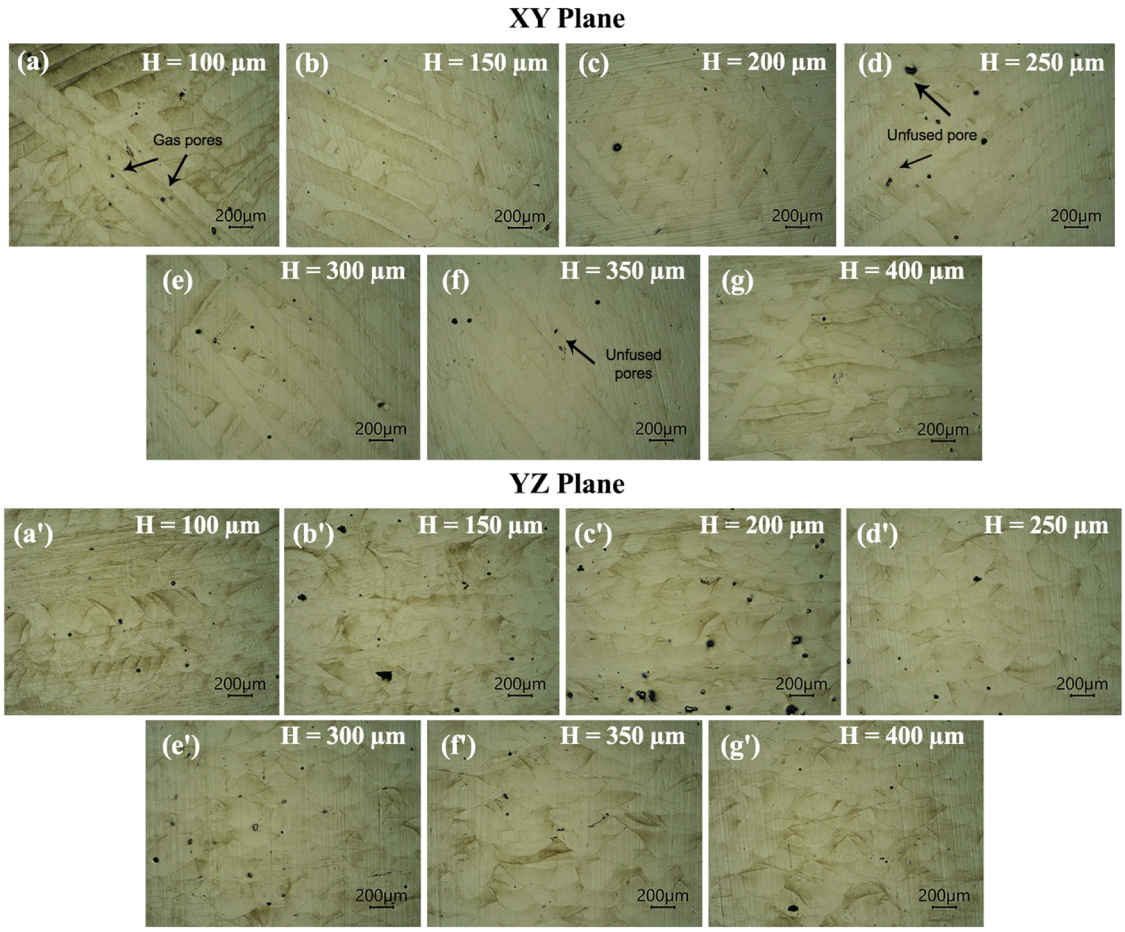

Fig. 2. Optical micrograph of as-built samples with P = 375 w, V = 200 mm/s, and different hatch spacing (a-g) of the XY plane, and (a'-g') melt pool morphology on the YZ plane.

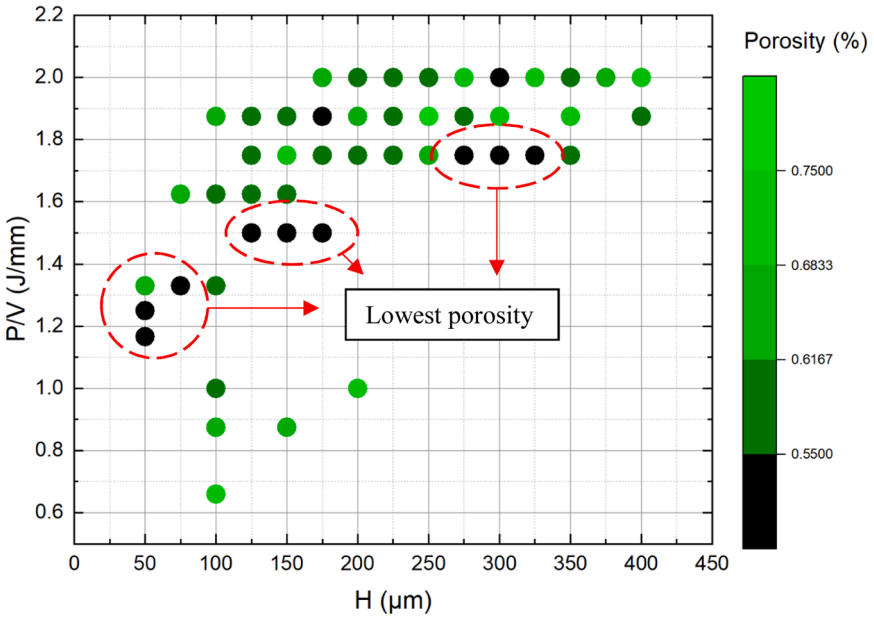

Fig. 3. Porosity percentage as a function of P/ V (J/mm) ratio and hatch spacing (µm).

direction, highlighting a distinct difference in grain structure compared to the conventional sample.

Fig. 5 displays the average grain size data, revealing a significant difference: while the conventional sample has a grain size of 19.8 µm, the sample fabricated with a 100 µm hatch spacing shows a much larger grain size of 54.8 µm. As hatch spacing increases, the grain size only

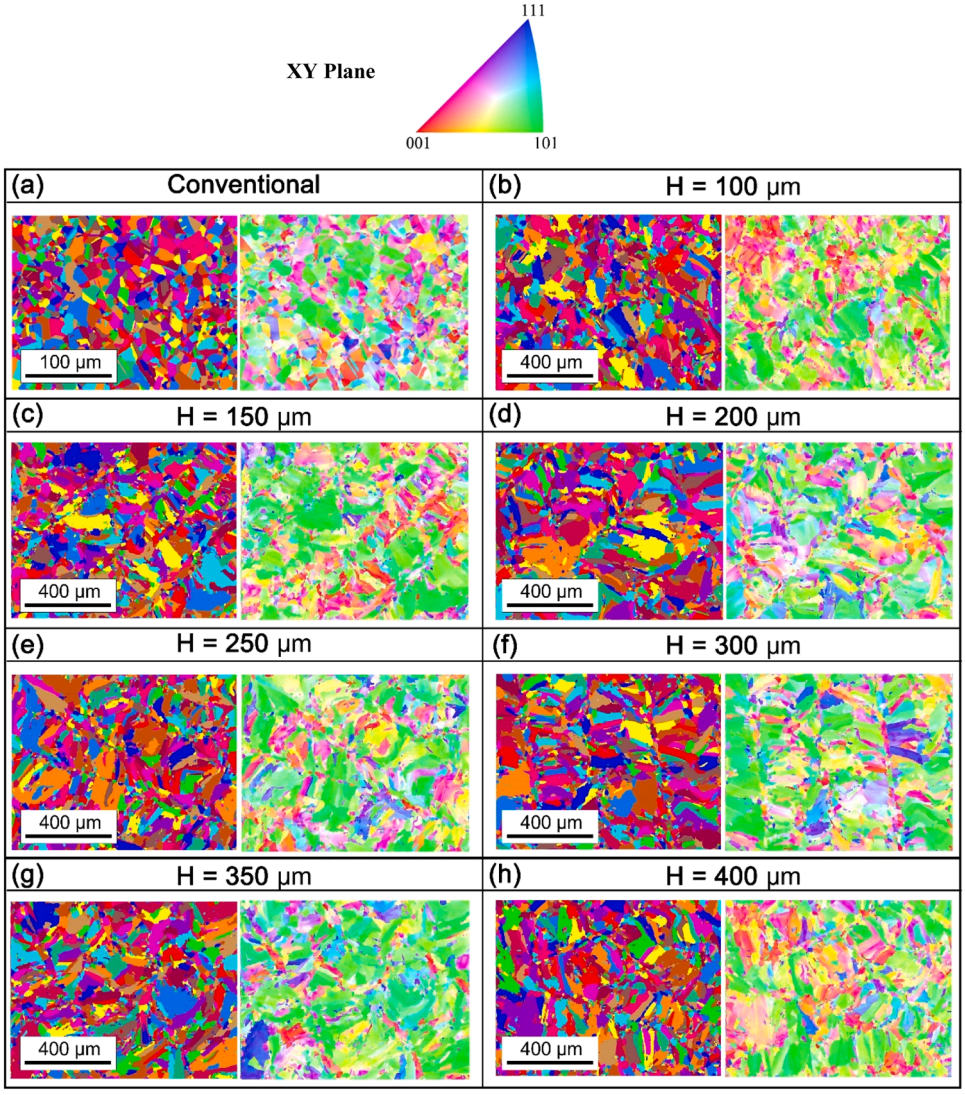

Fig. 4. Grain orientation map and inverse pole figure (IPF) of: (a) Conventional, and as-fabricated samples with P = 375 W, v = 200 mm/s and hatch spacing H of (b) 100 μm, (c) 150 μm, (d) 200 μm, (e) 250 μm, (f) 300 μm, (g) 350 μm and (h) 400 μm.

vary to a small extent, averaging around 60 μm.

The pole figure (PF) plots in Fig. 6 depict the texture strength distribution for the three plane families in the face-centered cubic (FCC) structure, specifically (001), (110), and (111). These plots reveal that among the three directions, the (110) texture component is the most dominant one. The statistical description of a fabric's intensity is quantified by the multiple of uniform density (MUD), which is derived from the highest intensity of the contoured pole figures [27]. In other words, the MUD number serves as an indicator of texture strength in an EBSD pole figure, higher values suggest stronger alignment. A MUD value of 1 indicates randomly aligned grains, whereas values significantly greater than 1 indicate a strong texture alignment [28]. According to Fig. 6, all as-fabricated samples had MUD values below 6. The sample fabricated with a 100 μm hatch spacing showed the highest MUD value at 5.12, indicating a relatively strong overall texture, although the (110) texture component itself was not particularly prominent. Conversely, the sample with a 400 μm hatch spacing had the lowest MUD value, around 3.72, reflecting a weaker texture.

The kernel average misorientation (KAM) and grain boundaries calculated from the EBSD analysis are illustrated in Fig. 7. The KAM provides a qualitative measure of the homogeneity of plastic deformation and the density of defects, such as dislocations, layered dislocations, and subgrain boundaries [29]. In Fig. 7a, the blue regions represent areas with the lowest misorientation angles and dislocation densities, indicating minimal lattice distortion. As the color transitions from blue to green, there is a corresponding increase in misorientation angles and dislocation densities. This progression shows the spatial distribution and intensity of these structural imperfections within the sample.

Fig. 7b illustrates that the sample printed with hatch spacing of 100 μm exhibited the lowest misorientation angle about 11.2°. This indicates a minimal dislocation density and small local plastic strains. Such minimal local plastic deformation is attributed to the low residual stresses caused by reduced thermal stresses during the as-fabricated printing process. Conversely, when the hatch spacing increased to 200 and 300 μm, the misorientation angle rose, reaching about 15–16 degrees, which corresponds to the highest dislocation density. This trend underscores the impact of hatch spacing on the distribution and intensity of dislocations within the material.

The phenomenon can be explained by the amount of heat input during the manufacturing process as hatch spacing increases, the heat input decreases. This reduction in heat input results in a higher density of dislocations associated with increased residual stress. Consequently, the accumulation of these defects and stresses will lead to better mechanical properties [29].

Increasing the hatch spacing beyond 300 μm leads to a decrease in misorientations. When the initial hatch spacing is small (H100),

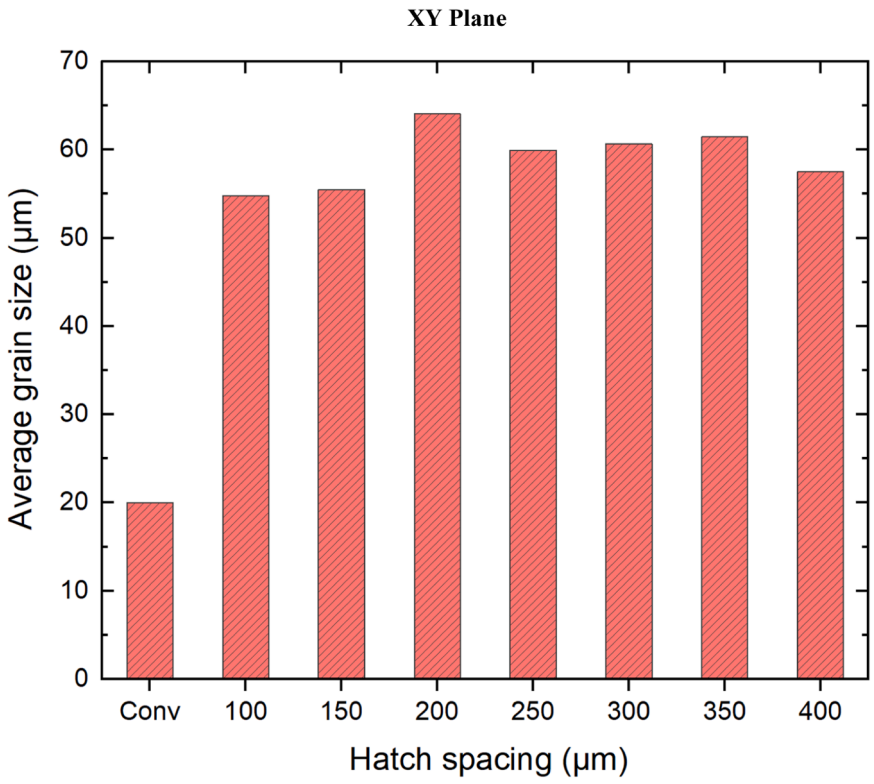

Fig. 5. Grain size variation of conventional and as-fabricated samples with P = 375 w, V = 200 mm/s and hatch spacing from 100 to 400 μm.

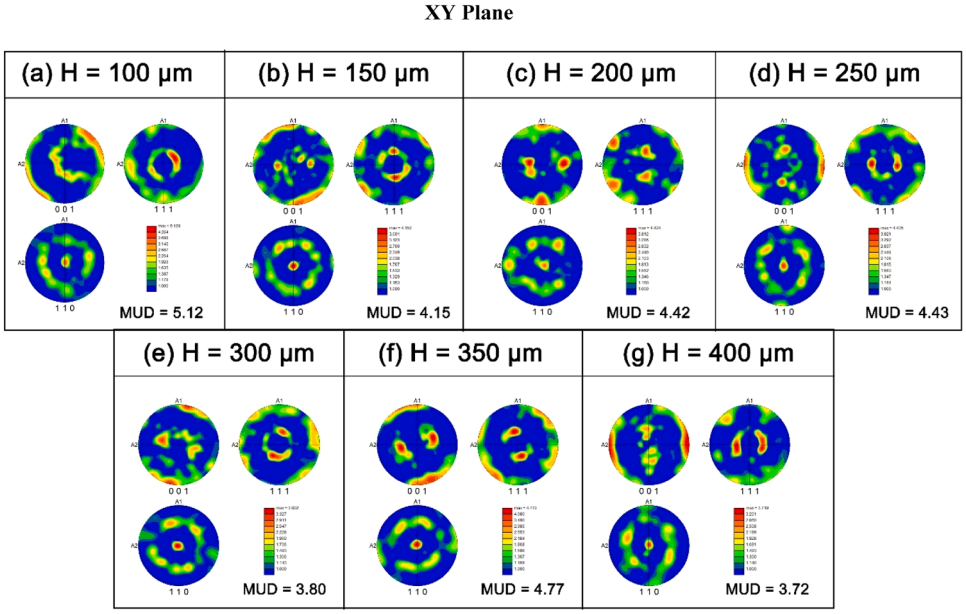

Fig. 6. Pole figures (PF) of as-fabricated samples with P = 375 W, V = 200 mm/s and different hatch spacing.

significant overlap between melt pools can occur, resulting in a more homogenized grain structure with lower misorientation. A small increase in spacing creates more separate melt pools, which permits some grain growth to occur independently within each pool. This can lead to an increase in misorientation (H300) compared to the highly homogenized case. As the hatch spacing continues to increase, the decrease in the thermal gradient will likely become the dominant effect. With larger spacing, the reduced interaction between melt pools leads to slower and more independent solidification, resulting a lower degree of misorientation between grains within each pool. This trend will likely outweigh the initial slight increase, leading to an overall decrease in KAM as the spacing continues to grow [29].

3.3. *Cyclic polarization*

Fig. 8a illustrates the cyclic polarization curves of both conventional and as-fabricated samples with varying hatch spacing after a 3-h immersion in 3.5 wt% NaCl. The curve for the as-fabricated samples

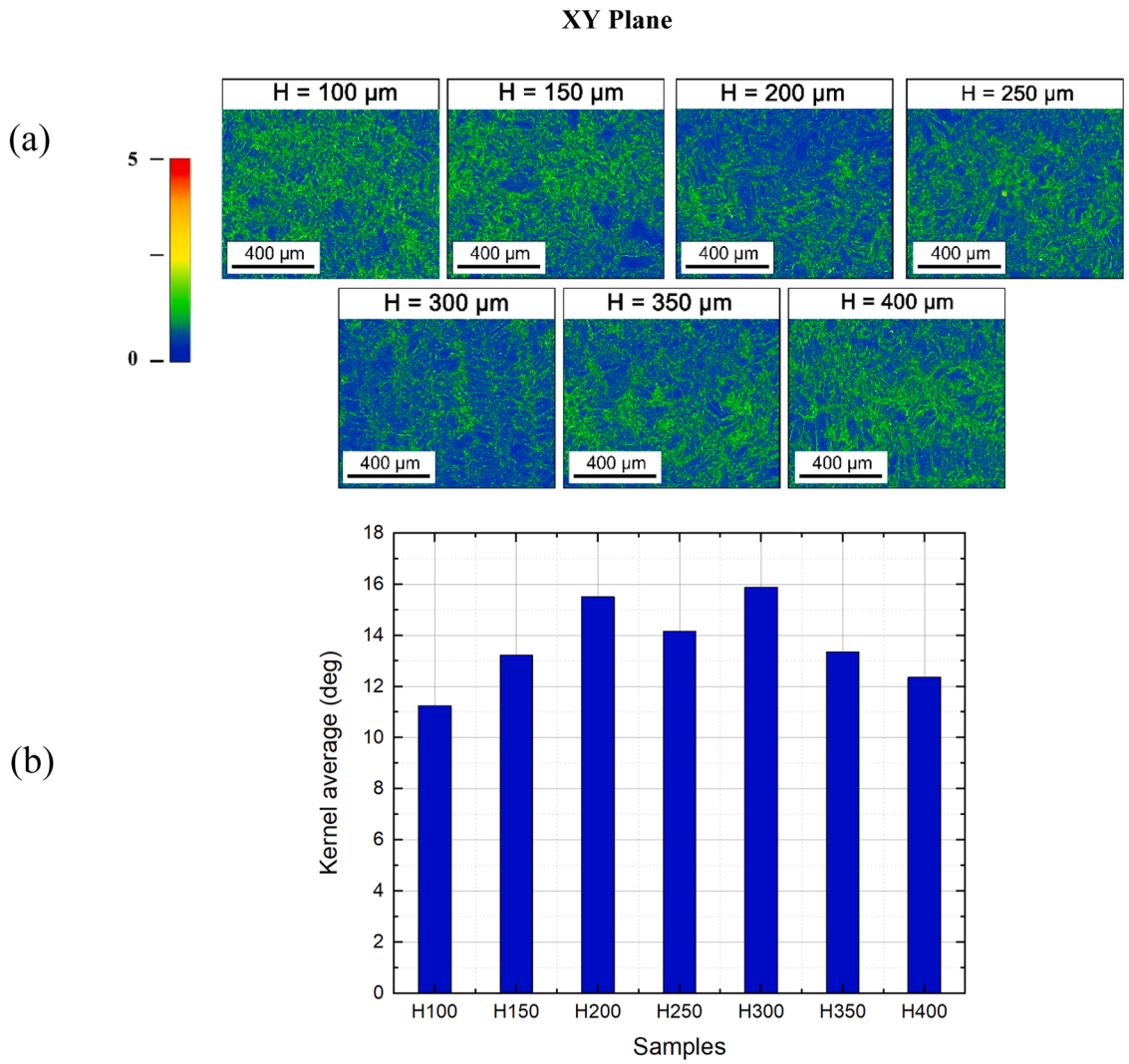

Fig. 7. Kernel average misorientation (KAM) maps and misorientation angle of as-fabricated samples with P = 375 W, V = 200 mm/s and different hatch spacing.

showed a slight positive shift compared to the conventional sample, suggesting a trend toward more noble potential values. When the potential shifts positively with respect to the open-circuit potential (OCP), an oxide protective layer forms on the surface, preventing a significant increase in corrosion current density (passive region). Further increasing the potential causes a drastic rise in current density due to film dissolution (transpassive region). The potential at which this occurs is known as the breakdown potential. As is evident in Fig. 8a, there are no anodic spikes in any of the curves. This suggest that the passive region is quite stable in Cu-Ni samples. After surpassing the breakdown potential, the current densities increased dramatically until the scanning direction changed upon reaching a current of $3.3 \times 10^{-3} A/cm^2$. As the potential decreased to more negative values, the reverse polarization curve intersected the forward polarization curve. This intersection point, known as the repassivation potential, which signifies the moment when the metal's surface regains its ability to form a protective oxide layer, effectively halting the progression of pitting corrosion. In other words, the repassivation potential demonstrates the material's capacity to repair itself and restore its protective properties even after initial corrosion damage [30]. The corrosion rate, breakdown, and repassivation potentials, derived from cyclic polarization, are presented in Fig. 8b, c, and d, respectively. The corrosion rate of the as-fabricated samples at OCP is approximately 125 nA/cm^2, which is marginally higher than that of the conventionally processed sample, measured at 80 nA/cm^2. According to Fig. 8c, the passive film on the conventional sample broke at −96 mV, whereas for the as-fabricated samples, it broke at roughly around −76 mV. This indicates that the passive layers formed on as-fabricated samples can withstand at higher potentials. Nevertheless, the as-fabricated samples experienced a higher corrosion rate in the passive region compared to the conventional sample. The conventional sample exhibited a current density of 0.2 $\mu A/cm^2$, whereas all the additively manufactured samples showed current densities of around 0.5 $\mu A/cm^2$. This difference suggests that while the LPBF conditions have higher breakdown potentials, there may be slight compromises in corrosion resistance within the passive region. Further investigation is required to fully understand the underlying causes and deeper insights into the long-term corrosion.

According to Fig. 8d, the repassivation potential for the as-fabricated samples averaged around −120 mV, whereas the conventional sample repassivated at −139 mV, implying that passivity breakdown occurred at a higher potential in the as-fabricated samples.

After the CPP test, there is the noticeable discoloration on the sample's surfaces (shown in Fig. 9), indicating the corrosion degradation on the entire sample surface. A closer examination also finds localized corrosion around the pores and fusion lines. To better examine the surfaces, they were cleaned with water, and as shown in Fig. 9a'-g', micropores are visible on all samples. Many of these pores existed before the test (as shown in Fig. 2) and they just became deeper and larger during the corrosion process. Among the samples with hatch spacings ranging from 100 to 400 microns, H400 sample exhibited pores with

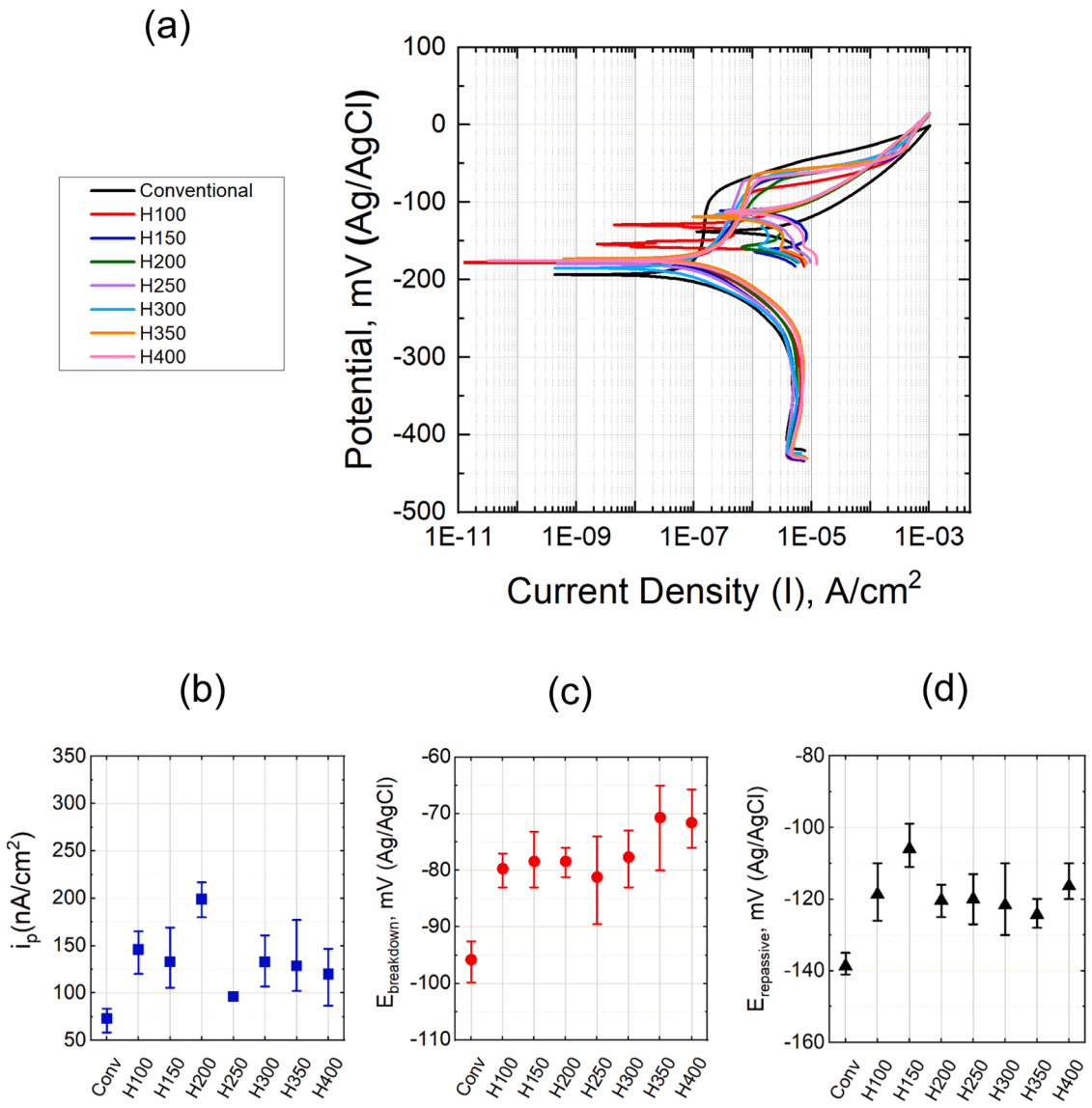

Fig. 8. Cyclic polarization curves for: (a) conventional and as-fabricated samples with P = 375 W, V = 200 mm /s and different hatch spacing, along with (b) corrosion, (c) breakdown and (d) repassivation potential.

larger diameters, some reaching up to 50 μm. This observation features the increased susceptibility to corrosion in samples with larger hatch spacings, where the formation of larger micropores is more pronounced. Notably, the shape of the molten paths is visible on some samples (H250 and H300), with the edges of these paths being more corroded by the sodium chloride solution compared to other areas.

3.4. EIS analysis

Fig. 10a and b displays the Nyquist and Bode plots for conventional and as-fabricated samples immersed in 3.5 wt% NaCl solution at room temperature. The diameter of the semicircles in Fig. 10a indicates the difficulty of electron transfer on the sample surface [31]. The sample with 400 μm hatch spacing exhibited the smallest semicircle radius, indicating the lowest resistance to electron transfer, whereas the samples with 150–200 μm hatch spacing along with the conventional showed the highest radius, suggesting greater resistance.

To model the electrochemical behavior, the equivalent circuit shown in Fig. 10c was employed. This circuit includes R_s (solution resistance), CPE_{ct} (constant phase element for the charge transfer-high frequency time constant), R_{ct} (charge transfer resistance), CPE_p (constant phase element for the passive layer-low frequency time constant), and R_p (resistance of the passive layer). The use of CPE terms instead of ideal capacitance accounts for the surface roughness, which prevents the sample from behaving as an ideal capacitor. The CPE provides a more accurate model by representing a capacitive element with a frequency-independent negative phase between current and voltage, interpolating between a capacitor and a resistor. The impedance value of the CPE can be calculated by the given equation [32]:

$$Z_{CPE} = Y_0^{-1}(j\omega)^{-n} \quad (1)$$

where Y_0 is the admittance constant, j is imaginary number and ω is the angular frequency which is equal to $2\pi f$. The parameter n is associated with surface roughness and typically falls within the range of −1 to 1. The fitted parameters are presented in Table 2. According to the equivalent circuit model, the corrosion process in the initial stage is governed by a combination of dielectric diffusion and electrochemical discharge. Upon exposure to a corrosive solution, a surface film forms an interface capacitor between the specimen substrate and the solution. Meanwhile, a double-layer capacitor forms between the ions of the solution and the film, and an equivalent circuit with two capacitors shows

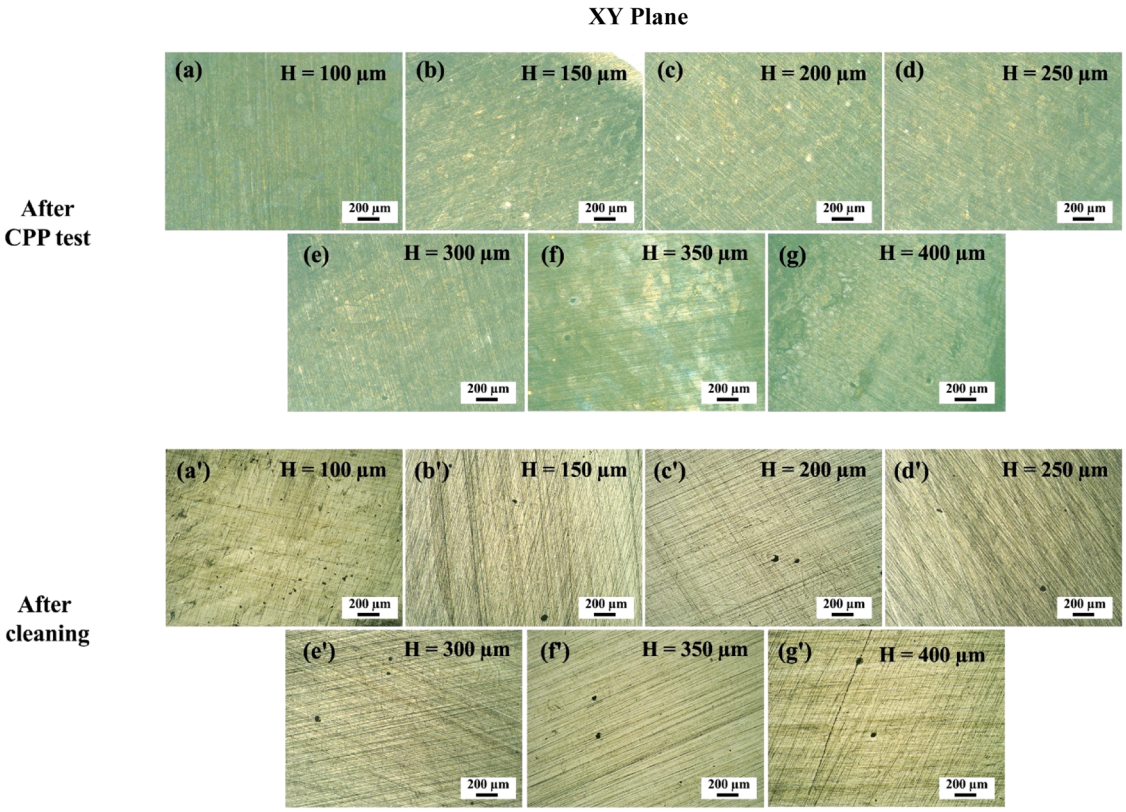

Fig. 9. OM images of specimens with P = 375 W, V = 200 mm/s, and different hatch spacing: (a-g) after CPP test (a'-g') after cleaning with water.

the appearance of a film layer resistance, R_f. In this case, the corrosion of alloy is composed of electron transfer and charge transport. Polarization resistance R_p characterizes the overall corrosion resistance of alloy, which is the sum of charge transfer resistance R_{ct} and film layer resistance R_f.

At the frequency of 10^{-2} Hz, the total resistance includes both the double-layer resistance and other components, such as the film layer resistance obtained from fitting data as a function of hatch spacing are shown in Fig. 10d and e, respectively. For comparison, the values for the conventional sample are depicted as horizontal lines. Accordingly, the conventional sample had an impedance value of 67 KΩ.cm^2 which was higher than most of the LPBF samples. However, among the as-fabricated samples, the impedance values follow the sequence: H400 < H350 < H300 < H250 < H100 < H200 < H150. In other words, samples H150 and H200 exhibit the highest impedance values even slightly higher than the conventional one. Consequently, these samples demonstrate superior corrosion resistance in sodium chloride solution compared to the other samples. The elevated impedance values for H150 and H200 suggest a more robust passive layer, enhancing their ability to withstand corrosive environments effectively. As evident in Fig. 10e, when hatch spacing increases from 100 to 400 µm, the charge transfer resistance initially reaches a maximum of 85–111 MΩ (H100 to H200) and then decreases to 42 MΩ (for H400). Fig. 11 presents the corrosion resistance at low frequency obtained from fitting data as a function of hatch spacing (H) and linear energy density (P/V). The samples with a P/V ratio between 1.7 and 2 J/mm and a hatch distance of 125–200 µm had the highest corrosion resistance (58–73 kΩ·cm^2). Deviations from these parameters resulted in decreased resistance. For instance, when the P/V ratio falls below 1 J/mm and the hatch spacing exceeds 250 µm, the samples display poor resistance to 3.5 wt% NaCl, with values nearly less than half of the best samples (28 – 43 kΩ·cm^2).

3.5. Mott Schottky

The formation and degradation of passive film on Cu-Ni are tied to the concentration of defects within the protective film. These processes are influenced by the electronic characteristics of the layers. Understanding these properties helps to explain how the films develop and deteriorate, providing insights into their protective capabilities and the conditions that can lead to their failure [33,34]. Mott Schottky (MS) experiments help elucidate the semiconducting properties of the protective layer by expressing the capacitance as a function of the applied potential.

$$\frac{1}{C^2} = \frac{2}{N_D \varepsilon \varepsilon_0 e}\left(E - E_{fb} - \frac{K_B T}{e}\right) \quad (2)$$

In this equation, e represents the electronic charge equal to 1.60×10^{-19} C, ε is the relative permittivity of n-type or p-type oxide layer, ε_0 denotes the vacuum permittivity (8.85×10^{-14} F cm^{-1}), K_B stands for the Boltzmann constant (1.38×10^{-23} J/K), and T is the temperature. By measuring the slope in MS plots, we can calculate the donor density (N_D), which primarily consists of oxygen vacancies in the oxide film.

Fig. 12 displays the MS and donor density plots for conventional and fabricated samples using LPBF with different hatch spacing in sodium chloride solution. As shown in Fig. 12a, all curves initially exhibit a negative slope before reaching a potential of −0.2 V, showing p-type behavior prior to entering the passivation region. When the potential goes beyond −0.2 V (moving into the passive region) the slope of the curves shifts from negative to positive, signaling a transition from p-type to n-type semiconductor behavior.

Concerning donor species, Macdonald et al. [35] proposed that the donors in the passive film consist of various defects such as cation, anion vacancies, and cation interstitials.

The donor density for the conventional sample has the lowest value at 1.8×10^{20} cm^3. In contrast, sample H100 exhibits a donor density of

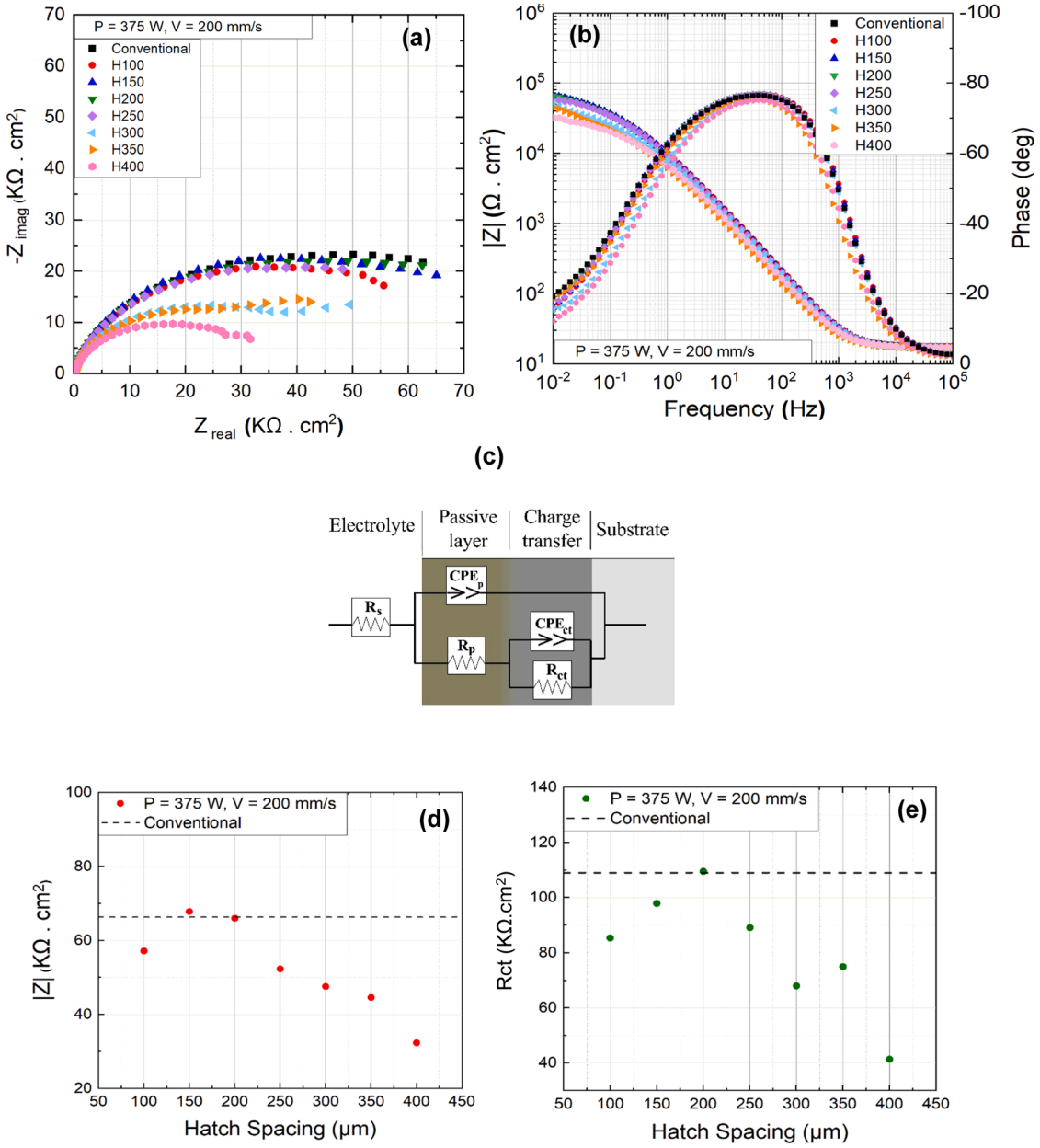

Fig. 10. EIS results for conventional and as-fabricated samples with P = 375 W, V = 200 mm/s and different hatch spacing: (a) Nyquist, (b) Bode, (c) Equivalent circuit, (d) Resistance at low frequency and (e) Double layer impedance obtained from fitting data.

Table 2
Obtained results from the proposed equivalent circuit.

Sample	R_s (Ω.cm^2)	R_P (Ω.cm^2)	n_P	CPE1 (μF.cm^{-2})	R_{ct} (KΩ.cm^2)	n_{ct}	CPE2 (μF.cm^{-2})
Conventional	17.43	9.07	0.907	14.38	109.10	0.382	17.22
H100	17.09	2.44	0.915	12.55	85.38	0.422	16.16
H150	17.07	22.61	0.912	13.31	97.86	0.409	15.66
H200	16.91	5.94	0.913	14.26	109.51	0.377	18.13
H250	17.16	1.78	0.911	14.09	89.10	0.409	17.88
H300	16.93	4.50	0.909	14.78	67.98	0.382	24.06
H350	17.03	2.08	0.901	21.76	74.97	0.359	32.69
H400	17.23	1.26	0.907	17.72	41.40	0.404	29.05

2.1×10^{20} cm^3. An upward trend in donor density was observed as the hatch spacing increases (Fig. 12b), reaching a maximum of 3.75×10^{20} cm^3 for H400 sample. This trend suggests that larger hatch spacings contribute to a higher concentration of defects, such as oxygen vacancies, within the films. The increasing donor density with wider hatch spacings indicates a greater presence of point defects, which could impact the electrochemical properties and stability of the passive layer.

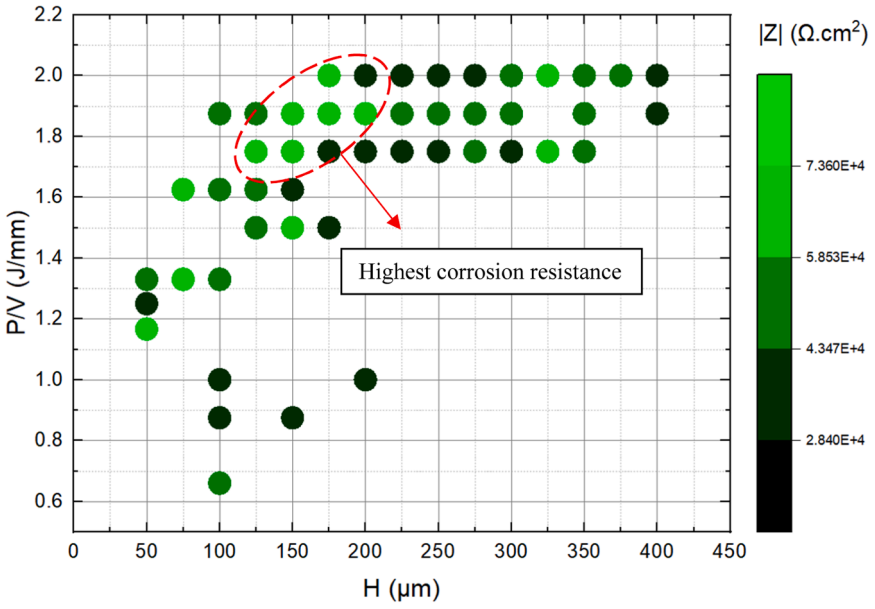

Fig. 11. Impedance values at the 10^{-2} Hz as a function of P/V (J/mm) ratio and hatch spacing H (μm) for all as-fabricated samples.

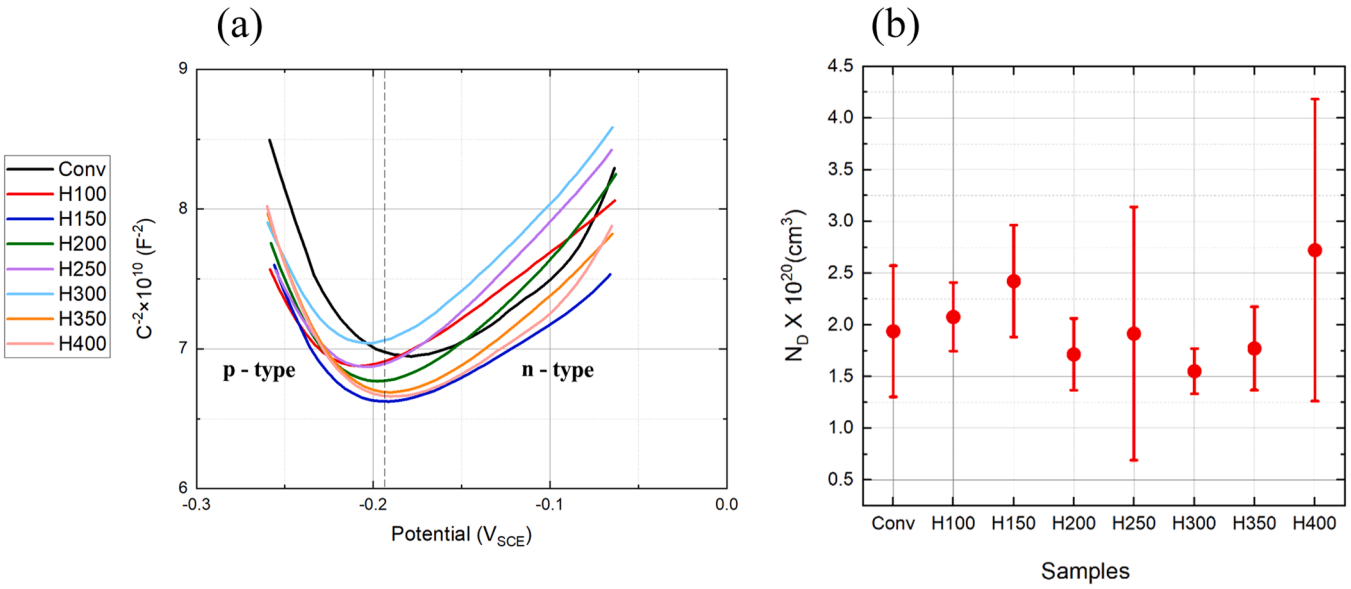

Fig. 12. (a) Mott-Schottky and (b) donor densities plots of conventional and as-fabricated samples with P = 375w, V = 200 mm/s and different hatch spacing.

4. Discussion

The parameters of the LPBF process have a complex impact on the quality of the fabricated samples, and numerous defects can arise from improper settings. Key parameters such as laser power, scanning speed, and hatch spacing significantly influence the size, shape, and thermal gradient of the molten pool. Modifying these parameters changes the thermal conditions during the manufacturing process, which in turn

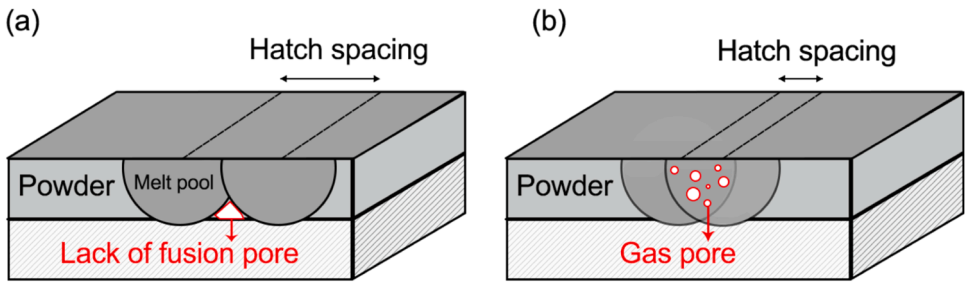

Fig. 13. Schematic of the pore formation mechanisms in LPBF.

affects the flow dynamics and stability of the molten pool. This can result in variations in the microstructure and properties of the final samples [13,16,36]. In Fig. 2, surface defects arise due to either insufficient or excessive input heat. As-printed sample with a hatch spacing of 150 μm had the lowest porosity percentage (PP < 0.5 %). This value experienced an uptrend when hatch spacing exceed 150 μm. As depicted in Fig. 13, when the hatch spacing increases, the distance between consecutive laser beams widens, resulting in the formation of unfused pores. This occurs because the laser beams are too far apart to adequately melt and fuse the material in between, leaving gaps and resulting in a porous structure [37,38]. Conversely, if the hatch spacing is too narrow, small pores appear on the surface due to the excessive overlap of laser paths (Fig. 13b). The excessive overlap can cause localized overheating and vaporization of the material, leading to the formation of micro-pores.

It is noteworthy to mention that in this study, all the examined as-fabricated samples exhibited a porosity percentage below 1 %. This low level of porosity indicates fewer voids, inclusions, and high density within the material, leading to better properties.

Thermal condition also can affect the grain size as seen in Fig. 5. Less heat means the molten material cools down quicker. In as-fabricated samples, with increasing hatch spacing from 100 to 400 μm there is an upward trend in grain size. The material cools faster between scans, but subsequent scans don't completely remelt the previously solidified regions. Therefore, incomplete melting during subsequent scans reduces the number of nucleation sites for new grains.

The corrosion properties of as-fabricated samples and conventional 70/30 Cu-Ni in 3.5 wt% NaCl at room temperature in this work showed that the passive layer has different behaviour which results in different corrosion resistance. As is shown in Fig. 8c, almost all as-fabricated samples have higher breakdown potentials compared to that of the conventional one. The reaction mechanism of film oxides on Cu-Ni is shown in Fig. 11.

The cathodic reaction in a natural solution is [39]:

$$O_2 + 2H_2O + 4e^- \rightarrow 4OH^- \quad (3)$$

In a chloride solution, Cu element mainly dissolve by forming $CuCl_2^-$ as the following [40]:

$$Cu + Cl^- \rightarrow e^- + CuCl \quad (4)$$

$$CuCl + Cl^- \rightarrow CuCl_2^- \quad (5)$$

It is worth mentioning that when the Cl^- concentration is high, $CuCl_2^-$ can be further coordinated to $CuCl_3^{2-}$ and $CuCl_4^{3-}$. Near the corrosion potential, the reactions are often thought to be reversible and subject to mixed regulation of mass transport and charge transfer. Afterwards, with the presence of H_2O and OH^- , the resultant soluble ion complex can also be hydrolysed and form cuprous oxide and cupric oxide [19,39,40]:

$$2CuCl_2^- + H_2O \rightarrow Cu_2O + 4Cl^- + 2H^+ \quad (6)$$

$$Cu_2O + H_2O + O_2 \rightarrow 2CuO + H_2O_2 \quad (7)$$

Localized acidity inside the film's pores might lead to the formation of a green corrosion product of copper hydroxychloride ($Cu_2(OH)_3Cl$) [41]. The inherent properties of nickel make the formed film more corrosion-resistant than copper oxide. This resistance is further enhanced by the greater incorporation of nickel into the copper oxide and hydroxide compounds. The reactions that produce these nickel compounds are as follows [19]:

$$Ni^{2+} + 2OH^- \rightarrow Ni(OH)_2 \quad (8)$$

$$Ni^{2+} + 2Cl^- \rightarrow NiCl_2 \quad (9)$$

$$NiCl_2 + 2OH^- \rightarrow H_2O + NiO + 2Cl^- \quad (10)$$

As immersion time increases, the Cu_2O film grows inward, enhancing the resistance and inhibiting iron dissolution, leading to a reduction in the corrosion rate. While the presence of metallic Fe in the corrosion product film of 70/30 Cu-Ni alloy in chloride solution is rare and its formation mechanism remains unclear, it may be formed through a mechanism similar to the redeposition of dissolved copper species [42]. MS analysis showed that in the passive region, the protective layers formed on the surface of the sample have n-type behaviour. According to the reactions carried out on the Cu-Ni surface that are mentioned above, this behavior can be attributed to the presence of FeO, $NiOH_2$ and most hydroxides. In contrast, before the samples enter the passive region, the Mott-Schottky diagram exhibits a negative slope, indicating p-type behavior. This behavior is characteristic of oxides such as Cu_2O and NiO [43,44]. Fig. 14

Porosity plays a critical role in influencing the corrosion behavior of as-fabricated materials. Increased porosity can lead to higher corrosion rates, as pores provide pathways for corrosive agents to penetrate the material's surface, undermining its passive layer and creating localized areas vulnerable to corrosion. However, low level of porosity (<0.5 %) have been reported not to adversely affect the corrosion performance of LPBF metals [12,45,46]. In this study, samples with optimized linear energy densities (1.1–1.75 J/mm) and moderate hatch spacings (50–325 μm) achieved lower porosity levels below 0.6 %, correlating with reduced void fraction and enhanced structural density. This lower porosity contributed to improved corrosion resistance by limiting access points for corrosive ions, supporting higher impedance values in EIS analysis, particularly for samples H150 and H200, which displayed the highest corrosion resistance. However, when hatch spacing exceeded this range, both porosity and susceptibility to corrosion increased, as indicated by lower charge transfer resistance values and higher current densities in the passive region.

Grain boundary and dislocations are also crucial factors influencing the corrosion behavior of LPBF fabricated samples. The grain boundaries and dislocation networks enhance the transport of passive layer constituents by providing pathways for higher diffusion rates. Elements like nickel (Ni), which have a strong propensity to form protective passive layers through reactions with oxygen, benefit from this increased diffusion. Even though the AM samples have larger grain size compared to conventional counterpart, they contain large amounts of dislocations as revealed by the EBSD analysis (Fig. 7). Consequently, ions are more effectively transported through these dislocation channels to the exposed surface, facilitating the nucleation of the passive film at numerous sites, leading to rapid thickening of the passive film. This is possibly responsible for the higher current density in the passive domain. The passive film will be more stable and repair more easily due to the more rapid transport of the anti-corrosion element to the surface, resulting in the observed higher breakdown and repassivation potentials compared to conventional counterpart.

The inward copper oxide along with nickel oxide which forms at a slow rate is considered the most protective and dense layer which can be related to the low-frequency region of EIS result (Fig. 11b) [6]. Since these layers gradually form at the final stage of immersion (Fig. 11c), immersion time is one of the most effective parameters. As a sample stays longer in the 3.5 wt% NaCl solution, the copper and nickel oxide layer becomes increasingly compact and thicker. This can be attributed to the reduction in surface cracks and defects, which promotes the formation of a more uniform oxide layer.

In future studies, it would be valuable to investigate the effects of longer immersion times on the corrosion behavior and passive film formation of as-fabricated samples. Further investigation on this topic could provide deeper insights into the long-term corrosion resistance and durability of components manufactured using the LPBF process. Additionally, understanding the dynamics of passive film growth over extended periods would contribute to optimizing the performance and reliability of LPBF-produced Cu-Ni alloy.

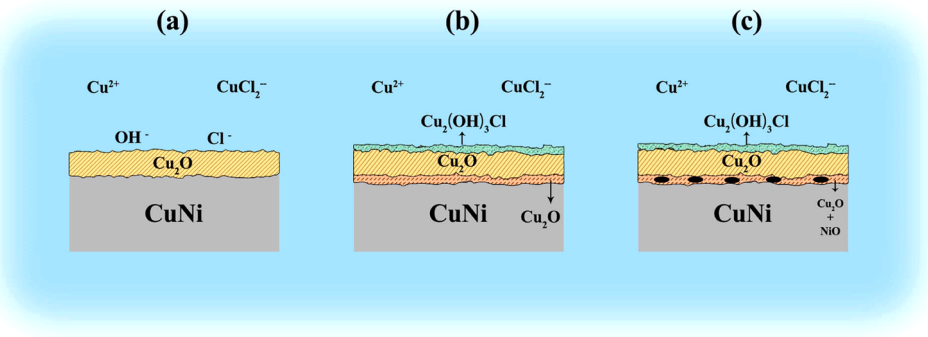

Fig. 14. Schematic diagrams of corrosion products after immersion in 3.5 wt% NaCl in 3 different steps.

5. Conclusion

In this investigation, the 70/30 Cu-Ni was effectively manufactured using LPBF technique. In order to have a broad evaluation of LPBF parameters on corrosion and microstructure properties, samples were fabricated in different ranges of power (300–400 W), scan rate (200–400 mm/s) and hatch spacing (50–400 μm). The properties of interest were compared to conventional Cu-Ni alloy. The microstructures and defects were analyzed using optical microscopy and EBSD, and the corrosion characteristics were analyzed using cyclic polarization and EIS technique in 3.5 wt% NaCl. The main conclusions are listed in the following:

1. All as-fabricated samples exhibit porosity percentages below 1 %, indicating the highly dense as-print structure and minimal presence of pores across the samples.
2. The grain size of as-fabricated samples is relatively larger than that of conventional sample. In addition, the as-fabricated samples primarily display elongated and irregular grain morphologies, with a predominant orientation in the $< 101 >$ crystallographic direction.
3. Although the corrosion rate is almost similar in both as-printed and wrought specimens, passive films created on the as-fabricated surface break down at higher potential than the conventional one and the repassivation ability is much stronger in as-fabricated samples. The as-fabricated samples show 30 % better performance in breakdown and repassivation. Also, it has been found that in as-printed samples with P = 375 W and V = 200 mm/s, the passive film tends to become weak when the hatch spacing exceeds a certain value (250 μm).
4. EIS analysis results show that the corrosion resistance of the best as-fabricated samples is almost similar to that of conventional, just slightly higher. This value is maximum (58 – 73 k Ω.cm^2) with hatch spacing between 125 and 200 μm and P/V ratio between 1.7 and 2 J/mm among all as-fabricated specimens in this work. As the parameters deviate further from this range, the resistance decreases accordingly. When the linear energy density (P/V) ratio drops below 1 J/mm and the hatch spacing exceeds 250 μm, the fabricated samples exhibit poor resistance to 3.5 wt% NaCl, with resistance values falling to nearly less than half of the best samples (28 – 43 kΩ·cm^2).
5. The passive film on the as-fabricated samples exhibits a relatively higher oxygen vacancy density compared to the wrought sample. The donor density is further increased with increasing hatch spacing and with a reduced influx of oxygen vacancies, the as-fabricated samples absorb aggressive ions like Cl^- and generate substantial cationic vacancies.

Funding

Office of Naval Research (Award No. N00014-21-1-2800); National Science Foundation (Award No. 2139383 and Award No. 2245107).

CRediT authorship contribution statement

Yao Fu: Conceptualization, Methodology, Supervision, Writing – review & editing. **Lin Cheng:** Writing – review & editing. **Jie Song:** Conceptualization, Methodology. **Mahdi Nadimi:** Data curation, Formal analysis, Writing – original draft, Writing – review & editing.

Declaration of Competing Interest

The authors declare that they have no known competing financial interests or personal relationships that could have appeared to influence the work reported in this paper.

Acknowledgments

The authors gratefully acknowledge the Office of Naval Research (Award No. N00014-21-1-2800) and National Science Foundation (Award No. 2139383 and Award No. 2245107) for providing the financial support. The authors also acknowledge the Advanced Research Computing at Virginia Tech for providing computational resources and technical support that have contributed to the results reported within this paper.

Data availability

The data described in this study are accessible upon request from the corresponding author.

References

[1] R. Francis, Effect of temperature on the corrosion of 70/30 copper–nickel in sea water, Br. Corros. J. 18 (1983) 35–39.
[2] S.J. Yuan, S.O. Pehkonen, Surface characterization and corrosion behavior of 70/30 Cu–Ni alloy in pristine and sulfide-containing simulated seawater, Corros. Sci. 49 (2007) 1276–1304.
[3] J.M. Popplewell, R.J. Hart, J.A. Ford, The effect of iron on the corrosion characteristics of 90-10 cupro nickel in quiescent 3·4%NaCl solution, Corros. Sci. 13 (1973) 295–309.
[4] A. Klassert, L. Tikana, Copper and copper–nickel alloys–an overview, Corros. Behav. Prot. Copp. Alum. Alloy. Seawater (2007) 47–61.
[5] R.J.K. Wood, S.P. Hutton, D.J. Schiffrin, Mass transfer effects of non-cavitating seawater on the corrosion of Cu and 70Cu-30Ni, Corros. Sci. 30 (1990) 1177–1201.
[6] L. Wu, A. Ma, L. Zhang, G. Li, L. Hu, Z. Wang, Y. Zheng, Erosion–corrosion behavior of 90/10 and 70/30 copper–nickel tubes in 1 wt% NaCl solution, Metals 13 (2023) 401.
[7] R.F. North, M.J. Pryor, The influence of corrosion product structure on the corrosion rate of Cu-Ni alloys, Corros. Sci. 10 (1970) 297–311.
[8] S. Hu, L. Liu, Y. Cui, Y. Li, F. Wang, Influence of hydrostatic pressure on the corrosion behavior of 90/10 copper-nickel alloy tube under alternating dry and wet condition, Corros. Sci. 146 (2019) 202–212.
[9] A. Vranić, N. Bogojevic, S. Ciric-Kostic, D. Croccolo, G. Olmi, Advantages and drawbacks of additive manufacturing, IMK-14 - Istrazivanje i razvoj 23 (2017) 57–62.

[10] J.Y. Lin, W.H. Cui, B. Han, H. Wang, X.H. Liu, Research on additive manufacturing technology in the field of mold repair, Mater. Sci. Forum 990 (2020) 61–66.
[11] T.D. Ngo, A. Kashani, G. Imbalzano, K.T.Q. Nguyen, D. Hui, Additive manufacturing (3D printing): a review of materials, methods, applications and challenges, Compos. Part B: Eng. 143 (2018) 172–196.
[12] J. Song, K. Sangoi, M. Nadimi, Y. Fu, Remarkably enhanced corrosion performance of 316 L stainless steel via laser powder bed fusion thin-layer deposition, Mater. Today Commun. 38 (2024) 107690.
[13] S. Cao, Y. Zou, C.V.S. Lim, X. Wu, Review of laser powder bed fusion (LPBF) fabricated Ti-6Al-4V: process, post-process treatment, microstructure, and property, Light: Adv. Manuf. 2 (2021) 313–332.
[14] Upadhyay, J.; Shoemaker, J.; Bernardin, J.; Kurennoy, S.; Lyles, J.; Bishofberger, K. Additive manufacturing of copper RF structures for particle accelerator applications in Proceedings of *Proceedings of the 14th International Particle Accelerator Conference, Venice, Italy*, (2023).
[15] S. Yadav, C. Paul, A. Jinoop, A. Rai, K. Bindra, Laser directed energy deposition based additive manufacturing of copper: process development and material characterizations, J. Manuf. Process. 58 (2020) 984–997.
[16] S. Chowdhury, N. Yadaiah, C. Prakash, S. Ramakrishna, S. Dixit, L.R. Gupta, D. Buddhi, Laser powder bed fusion: a state-of-the-art review of the technology, materials, properties & defects, and numerical modelling, J. Mater. Res. Technol. 20 (2022) 2109–2172.
[17] Q. Chen, Y. Fu, A.C. To, Multiphysics modeling of particle spattering and induced defect formation mechanism in Inconel 718 laser powder bed fusion, Int. J. Adv. Manuf. Technol. 123 (2022) 783–791.
[18] B. Gnanasekaran, J. Song, V. Vasudevan, Y. Fu, Corrosion fatigue characteristics of 316L Stainless steel fabricated by laser powder bed fusion, Metals 11 (2021) 1046.
[19] W.A. Badawy, K.M. Ismail, A.M. Fathi, Effect of Ni content on the corrosion behavior of Cu–Ni alloys in neutral chloride solutions, Electrochim. Acta 50 (2005) 3603–3608.
[20] O.O. Ekerenam, A.-L. Ma, Y.-G. Zheng, S.-Y. He, P.C. Okafor, Evolution of the corrosion product film and its effect on the erosion–corrosion behavior of two commercial 90Cu–10Ni tubes in seawater, Acta Metall. Sin. (Engl. Lett.) 31 (2018) 1148–1170.
[21] Y. Miao, C. Li, Y. Zhao, Y. Wu, J. Liu, Z. Wang, B. Zhang, Material properties of gradient copper-nickel alloy fabricated by wire arc additive manufacturing based on bypass-current PAW, J. Manuf. Process. 83 (2022) 637–649.
[22] J. Song, X.A. Jimenez, A.C. To, Y. Fu, Microstructures and corrosion properties of wire arc additive manufactured copper–nickel alloys, Materials 17 (2024) 876.
[23] J. Mertz, Introduction to optical microscopy, Cambridge University Press, 2019.
[24] M.M. Nowell, R.A. Witt, B.W. True, EBSD sample preparation: techniques, tips, and tricks, Microsc. Today 13 (2005) 44–49.
[25] T. Ronneberg, C.M. Davies, P.A. Hooper, Revealing relationships between porosity, microstructure and mechanical properties of laser powder bed fusion 316L stainless steel through heat treatment, Mater. Des. 189 (2020) 108481.
[26] B. Feng, C. Wang, Q. Zhang, Y. Ren, L. Cui, Q. Yang, S. Hao, Effect of laser hatch spacing on the pore defects, phase transformation and properties of selective laser melting fabricated NiTi shape memory alloys, Mater. Sci. Eng.: A 840 (2022) 142965.
[27] O. Gokcekaya, T. Ishimoto, T. Todo, R. Suganuma, R. Fukushima, T. Narushima, T. Nakano, Effect of scan length on densification and crystallographic texture formation of pure chromium fabricated by laser powder bed fusion, Crystals 11 (2020) 9.
[28] P. Bland, L. Howard, D. Prior, J. Wheeler, R. Hough, K. Dyl, Earliest rock fabric formed in the Solar System preserved in a chondrule rim, Nat. Geosci. 4 (2011).
[29] S.-S. Rui, Q.-N. Han, X. Wang, S. Li, X. Ma, Y. Su, Z. Cai, D. Du, H.-J. Shi, Correlations between two EBSD-based metrics Kernel Average Misorientation and Image Quality on indicating dislocations of near-failure low alloy steels induced by tensile and cyclic deformations, Mater. Today Commun. 27 (2021) 102445.
[30] S. Esmailzadeh, M. Aliofkhazraei, H. Sarlak, Interpretation of cyclic potentiodynamic polarization test results for study of corrosion behavior of metals: a review, Prot. Met. Phys. Chem. Surf. 54 (2018) 976–989.
[31] M. Metikoš-Huković, R. Babić, I. Škugor, Z. Grubač, Copper–nickel alloys modified with thin surface films: corrosion behaviour in the presence of chloride ions, Corros. Sci. 53 (2011) 347–352.
[32] Z.-G. Ye, H.-M. Meng, D.-B. Sun, Electrochemical impedance spectroscopic (EIS) investigation of the oxygen evolution reaction mechanism of Ti/IrO2+MnO2 electrodes in 0.5m H2SO4 solution, J. Electroanal. Chem. 621 (2008) 49–54.
[33] Y. Cui, L. Chen, L. Wang, J. Cheng, L. Zhang, Response of the metastable pitting corrosion of laser powder bed fusion produced Ti–6Al–4V to H+ concentration changes, Metals 13 (2023) 514.
[34] S.R. Trisnanto, X. Wang, M. Brochu, S. Omanovic, Effects of crystallographic orientation on the corrosion behavior of stainless steel 316L manufactured by laser powder bed fusion, Corros. Sci. 196 (2022) 110009.
[35] D.D. Macdonald, M. Urquidi-Macdonald, Theory of steady-state passive films, J. Electrochem. Soc. 137 (1990) 2395.
[36] Y.-W. Cui, L.-Y. Chen, P. Qin, R. Li, Q. Zang, J. Peng, L. Zhang, S. Lu, L. Wang, L.-C. Zhang, Metastable pitting corrosion behavior of laser powder bed fusion produced Ti-6Al-4V in Hank's solution, Corros. Sci. 203 (2022) 110333.
[37] L. Li, Y. Gou, W. Zhang, X. Meng, H. Zhang, P. Li, S. Huang, J. Zhou, Effect of hatch spacing on the characteristics of LPBF 2195 Al-Li alloy, J. Alloy. Compd. 972 (2024) 172804.
[38] J. Wang, R. Zhu, Y. Liu, L. Zhang, Understanding melt pool characteristics in laser powder bed fusion: an overview of single- and multi-track melt pools for process optimization, Adv. Powder Mater. 2 (2023) 100137.
[39] G. Kear, B.D. Barker, K. Stokes, F.C. Walsh, Electrochemical corrosion behaviour of 90—10 Cu—Ni alloy in chloride-based electrolytes, J. Appl. Electrochem. 34 (2004) 659–669.
[40] J. Mathiyarasu, N. Palaniswamy, V.S. Muralidharan, Electrochemical behaviour of copper-nickel alloy in chloride solution, Proc. / Indian Acad. Sci. 111 (1999) 377–386.
[41] X. Gao, M. Liu, Corrosion behavior of high-strength C71500 copper-nickel alloy in simulated seawater with high concentration of sulfide, Materials 15 (2022) 8513.
[42] A.L. Ma, S.L. Jiang, Y.G. Zheng, W. Ke, Corrosion product film formed on the 90/10 copper–nickel tube in natural seawater: composition/structure and formation mechanism, Corros. Sci. 91 (2015) 245–261.
[43] M. Nolan, S. Elliott, The p-type conduction mechanism in Cu2O: a first principles study, Phys. Chem. Chem. Phys.: PCCP 8 (2006) 5350–5358.
[44] R. Molaei, R. Bayati, J. Narayan, Crystallographic characteristics and p-type to n-type transition in epitaxial NiO thin film, Cryst. Growth Des. 13 (2013) 5459–5465.
[45] B. Gnanasekaran, J. Song, V. Vasudevan, Y. Fu, Corrosion fatigue characteristics of 316L stainless steel fabricated by laser powder bed fusion, Metals 11 (2021) 1046.
[46] G. Sander, V. Cruz, M. Jurg, N. Birbilis, X. Gao, M. Brameld, C. Hutchinson, On the corrosion and metastable pitting characteristics of 316L stainless steel produced by selective laser melting, J. Electrochem. Soc. 164 (2017) C250–C257.